Applied Physics B (2024) 130:133
https://doi.org/10.1007/s00340-024-08270-5

Applied Physics B
Lasers and Optics

RESEARCH

High-speed single-frame polarimeter for thermal radiation to measure the 3D geometry of hot metal surfaces

Michael Sawannia[1] · Peter Berger[1] · Rudolf Weber[1] · Christian Hagenlocher[1] · Thomas Graf[1]

Received: 31 January 2024 / Accepted: 24 June 2024 / Published online: 5 July 2024

Abstract
The 3D geometry of the interaction zone in laser material processing is of major importance as it defines the absorption of the laser beam and may influence the hydrodynamics of the process. With the aim of measuring this geometry, which typically changes with frequencies in the order of 10 kHz, a single-frame polarimeter with acquisition rates of up to 75 kHz is presented in this work. It simultaneously records four images of the thermal process emission, through four linear polarizers with different orientations. The formulae required for the reconstruction of the 3D geometry from these images are derived and validated on an example of a heated steel sphere. The reconstructed geometry was found to be in good agreement with the examined sphere. An experimental example is also given of the application of this technology to geometry measurement of a highly dynamic laser cutting front at a framerate of 75 kHz.

1 Introduction

In laser cutting and laser welding the shapes of the cutting fronts and the welding capillaries have a significant influence on the processing result [1–4]. To determine the surface geometry during the process, standard measuring methods such as three-dimensional (3D) coordinate measuring devices cannot be used, and optical coherence tomography (OCT) is not fast enough to capture the complete 3D shape of the processing front. X-ray observation during the machining process is possible [5, 6], but the current limits of the temporal resolution of about 1 kHz are too low to resolve the fluctuations on the processing front.

Our approach to determine the 3D shape of the surface is to apply imaging polarimetry, which exploits the angle-dependent emissivity of the thermal radiation according to Fresnel's equations. The polarization of reflected, transmitted or emitted light carries information about the complex refractive index of the interacting material and the angle of incidence or emission [7], which allows the determination of the 3D-orientation of a thermally radiating surface when the complex refractive index of the emitting material is known. Imaging polarimeters are divided into active systems, which illuminate an object with polarized radiation, and passive systems, which analyze the reflection of natural light (sun) or the emission from the investigated surface [8]. Vapor capillaries with high aspect ratios which are formed during laser welding absorb most of the incident radiation, which makes it difficult to measure their geometries with active polarimeters. A passive approach, that exploits the polarized thermal emission from the hot processing front was therefore applied for our investigations.

An attempt using a similar approach has already been presented in [9]. However, as a result of the limited camera performance and the restricted optical aperture used, the framerate in this case was limited to several 100 Hz, which is far too low for the detection of the very rapid geometrical changes which take place on a laser processing front.

With slightly modified versions of the single-frame polarimeter presented in the following work, the present authors have been able to perform imaging polarimetry with frame rates of up to 75 kHz to investigate the shape of the cutting front during the laser cutting process [10–12] or capillaries during electron beam welding [13]. The present paper provides the underlying theory with the applicable formulas and their derivation. The high-speed polarimeter that has been developed is presented, and its validation demonstrated using a heated sphere.

✉ Michael Sawannia
michael.sawannia@ifsw.uni-stuttgart.de

[1] Institut für Strahlwerkzeuge (IFSW), Universität Stuttgart, Stuttgart, Germany

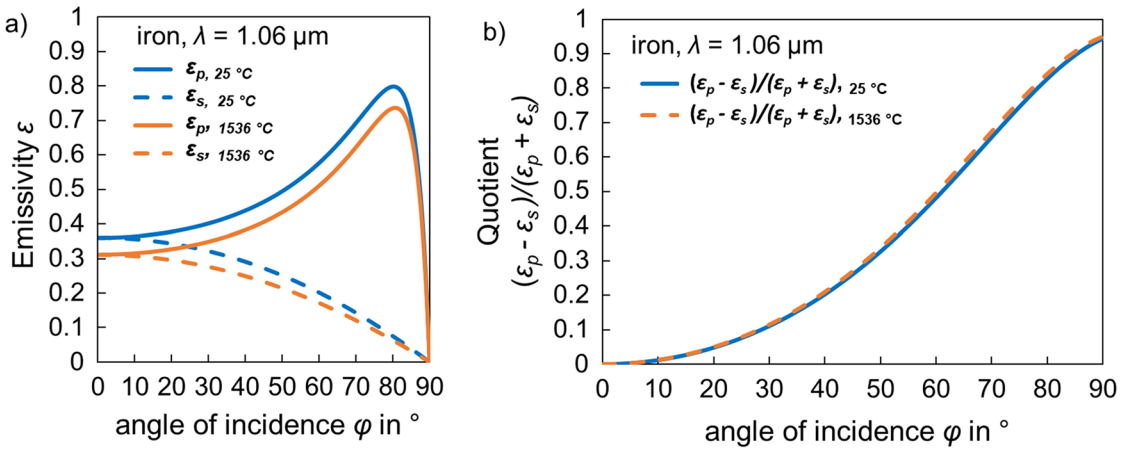

Fig. 1 **a** Angular dependence of the emissivities of solid iron (blue) at a temperature of 25 °C with n = 3.9 and k = 4.4 and liquid iron (orange) at the melting temperature of 1536 °C with n = 3.6 and k = 5.0 at a wavelength of λ = 1.06 µm, values for n and k from [16]. **b** Angular dependence of the quotient $Q = (\varepsilon_p - \varepsilon_s)/(\varepsilon_p + \varepsilon_s)$ for both temperatures

2 Theory

According to Kirchhoff's law of thermal radiation, the emissivity ε in thermal equilibrium equals the absorptivity A [7] and can therefore be expressed by the Fresnel equations. Provided that $n^2 + k^2 >> 1$, the Fresnel equations for the absorptivity may be approximated by

$$\varepsilon_p(\varphi) = A_p(\varphi) = \frac{4 \cdot n \cdot \cos(\varphi)}{\left(n^2 + k^2\right) \cdot \cos^2(\varphi) + 2 \cdot n \cdot \cos(\varphi) + 1}, \tag{1}$$

for p polarization and

$$\varepsilon_s(\varphi) = A_s(\varphi) = \frac{4 \cdot n \cdot cos(\varphi)}{\left(n^2 + k^2\right) + 2 \cdot n \cdot cos(\varphi) + \cos^2(\varphi)}, \tag{2}$$

for s polarization, where n and k are the real and imaginary part of the complex refractive index $n \pm ik$, respectively (the sign of the imaginary part depends on convention but is of no relevance for the following), and φ is the angle of incidence or polar angle (with respect to the surface's normal) [14, 15]. The angular dependence of the emissivities at a wavelength of λ = 1.06 µm is shown in Fig. 1 (a) for solid iron at room temperature and liquid iron at melting temperature. For the case that the requirement $n^2 + k^2 >> 1$ does not apply, a method using the exact Fresnel equations is described later in the paper.

While the absolute values of the emissivities significantly depend on the actual temperature, the quotient

$$Q(\varphi) = \frac{\varepsilon_p(\varphi) - \varepsilon_s(\varphi)}{\varepsilon_p(\varphi) + \varepsilon_s(\varphi)} \tag{3}$$

exhibits a negligible temperature dependence as shown by Fig. 1b. Due to the uniqueness of the curves $Q(\varphi)$ this quotient allows us to determine the polar angle by analyzing the polarization of the emitted radiation when the complex refractive index is known. This approach has already been shown to be viable for the determination of both the rapidly fluctuating inclination of laser cutting fronts [17] and the geometry of vapor capillaries during laser welding [18].

As shown in Fig. 2, the orientation of a surface element (blue) in the 3D space can be specified by the polar angle φ (cyan) and the azimuthal angle α (red) of it's normal vector $\vec{n}$ (dark blue) in a spherical coordinate system. The orientation of a surface element is unambiguously describable within the ranges $0° \leq \varphi \leq 90°$ and $-180° \leq \alpha < 180°$.

For the sake of simplicity, the axis with $\varphi = 0°$ is chosen to coincide with the camera's line of vision, the origin of the coordinate system being on the analyzed surface. The transmissivity of the polarizer is given by $\cos^2(\alpha - \beta)$ and $\sin^2(\alpha - \beta)$ for the p- and the s-polarized thermal emission of the surface, respectively, where β (purple) is the orientation of the polarizer [19]. The intensity I_β of the thermal emission of the surface element which is transmitted through the linear polarizer is therefore proportional to

$$I_\beta(\varphi, \alpha) \propto \varepsilon_p(\varphi) \cdot \cos^2(\alpha - \beta) + \varepsilon_s(\varphi) \cdot \sin^2(\alpha - \beta). \tag{4}$$

Hence, when $\alpha = \beta$ or $\alpha = \beta \pm 180°$, only the p-polarized emission of the surface is transmitted through the polarizer, whereas only the s-polarized emission is transmitted when $|\alpha - \beta| = 90°$.

The angles φ and α can be derived from one single measurement recording the intensities I_β transmitted through four linear polarizers with the orientations $\beta = 0°$, 45°, 90°, and 135° using the quotients

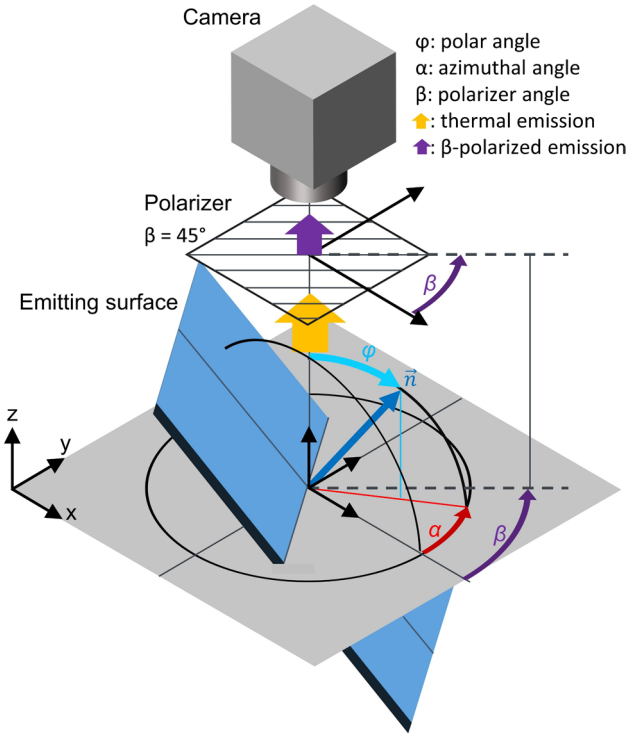

Fig. 2 Orientation of a plane surface element in the 3D space. The thermal radiation emitted from the surface is transmitted through a polarizer with the orientation β and is recorded by a camera whose line of vision defines the axis with $\varphi = 0°$

$$Q_1(\varphi,\alpha) = \frac{I_{0°}(\varphi,\alpha) - I_{90°}(\varphi,\alpha)}{I_{0°}(\varphi,\alpha) + I_{90°}(\varphi,\alpha)} = \frac{\varepsilon_p(\varphi)\cdot cos(2\alpha) - \varepsilon_s(\varphi)\cdot\cos(2\alpha)}{\varepsilon_p(\varphi) + \varepsilon_s(\varphi)} \tag{5}$$

and

$$Q_2(\varphi,\alpha) = \frac{I_{45°}(\varphi,\alpha) - I_{135°}(\varphi,\alpha)}{I_{45°}(\varphi,\alpha) + I_{135°}(\varphi,\alpha)} = \frac{\varepsilon_p(\varphi)\cdot sin(2\alpha) - \varepsilon_s(\varphi)\cdot\sin(2\alpha)}{\varepsilon_p(\varphi) + \varepsilon_s(\varphi)}, \tag{6}$$

where the common trigonometric relationships are used. Figure 3 shows the two quotients $Q_1(\varphi,\alpha)$ and $Q_2(\varphi,\alpha)$ as a function of the polar angle and the azimuthal angle. The material constants used were $n = 2.95$ and $k = 3.48$ for iron at the wavelength of $\lambda = 857$ nm [20], which are later used for the 3D-reconstruction.

The values of $Q_1(\varphi,\alpha)$ and $Q_2(\varphi,\alpha)$ can range between − 1 to 1, depending on the material. The dependence of $Q_2(\varphi,\alpha)$ equals the one $Q_1(\varphi,\alpha)$ except that it is shifted by 45° with respect to the azimuthal angle α. In Fig. 3 a given value of each quotient $Q_1(\varphi,\alpha)$ and $Q_2(\varphi,\alpha)$ corresponds to one contour line, indicated by the red line for the example $Q_1 = 0.5$ and the cyan line for $Q_2 = 0.5$. The intersection of the two contour lines gives the angles φ and α of the observed surface element. Since $-180° \le \alpha < 180°$ the 180° periodicity of Q_1 and Q_2 in α results in an ambiguity with two possible pairs of angles leading to the same values of the two quotients. This is why additional information on

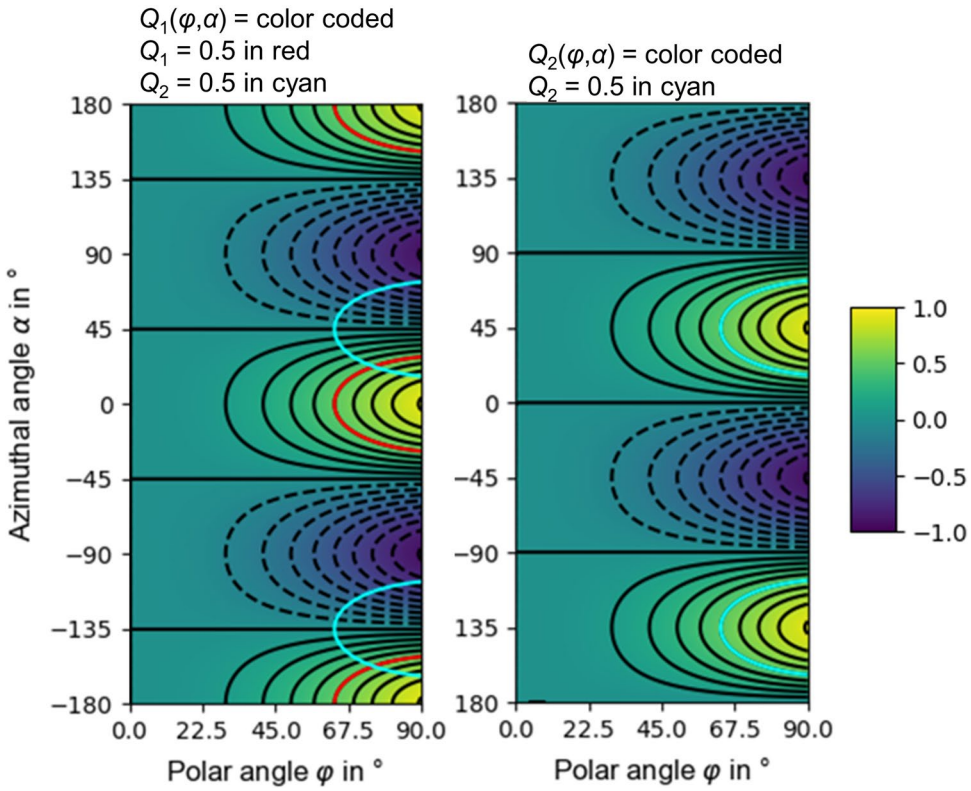

Fig. 3 The quotient $Q_1(\varphi,\alpha)$ and quotient $Q_2(\varphi,\alpha)$ plotted as a function of the polar angle and the azimuthal angle, for steel with the refractive index $n = 2.95$ and extinction coefficient $k = 3.48$ for the wavelength $\lambda = 857$ nm. The black lines are contour lines (dashed for negative values). The red line equals $Q_1 = 0.5$. The cyan line equals $Q_2 = 0.5$

the properties of the observed surface is needed to decide which of the two pairs of angles applies. In practice it is generally known whether the observed surface is mainly concave or convex and one may restrict the possible range of α to $-90° \le \alpha < 90°$, within which only one unambiguous pair of angles exists for given values of Q_1 and Q_2. From the experimentally determined values of the quotients Q_1 and Q_2, the angles may be found by using look-up tables for $Q_1(\varphi, \alpha)$ and $Q_2(\varphi, \alpha)$. For materials for which the approximation criteria $n^2 + k^2 >> 1$ does not apply, the terms $\varepsilon_p(\varphi)$ and $\varepsilon_s(\varphi)$ in Eqs. (5) and (6) can be replaced by the exact Fresnel equations in this look-up approach.

Rather than using look-up tables, the angles $0° \le \varphi \le 90°$ and $-90° \le \alpha < 90°$ can also be determined from analytical expressions by using the approximate Fresnel equations given in (1) and (2) and the Eqs. (5) and (6). As shown in the appendix A, the azimuthal angle α calculated from measured values $\hat{Q}_1$ and $\hat{Q}_2$ of the quotients $Q_1(\varphi, \alpha)$ and $Q_2(\varphi, \alpha)$ is found to be independent of φ and is given by

$$\alpha = \frac{atan2\left(\frac{\hat{Q}_2}{\hat{Q}_1}\right)}{2}, \tag{7}$$

where the atan2 function is used, as for instance described in [21]. The azimuthal angle α resulting from the values of $\hat{Q}_1$ and $\hat{Q}_2$, as e. g. determined from a measurement, is plotted in Fig. 4a. It can be seen from this result that for azimuthal angles with values close to ± 90°, a small variation of $\hat{Q}_2$ leads to an abrupt change of the sign of α, which in practice represents a problem for the correct 3D reconstruction of the analyzed surfaces.

The derivation of the analytical expression for the polar angle φ is shown in appendix B.

By using

$$r = \sqrt{\hat{Q}_1^2 + \hat{Q}_2^2} \tag{8}$$

the polar angle φ in the range of $0° \le \varphi \le 90°$ is found to be

$$\varphi(r) = arccos\left(\frac{-2 \cdot r \cdot n + \sqrt{4n^2r^2 - \left(\mathrm{r} \cdot \left(1 + n^2 + k^2\right) - (1 - n^2 - k^2)\right) \cdot \left(\mathrm{r} \cdot \left(1 + n^2 + k^2\right) + \left(1 - n^2 - k^2\right)\right)}}{\mathrm{r} \cdot \left(1 + n^2 + k^2\right) - (1 - n^2 - k^2)} \right). \tag{9}$$

The polar angle φ resulting from the values of $\hat{Q}_1$ and $\hat{Q}_2$ is plotted in Fig. 4b. Each combination of $\hat{Q}_1$ and $\hat{Q}_2$ unambiguously yields one value of φ.

As seen from Fig. 4b, the geometry can be reconstructed with confidence in the range $15° < \varphi < 75°$. For polar angles with $\varphi < 15°$ the value of φ is very sensitive to small changes of the measured values $\hat{Q}_1$ and $\hat{Q}_2$ and its accuracy is therefore influenced by the noise of the camera. In the range of $75° \le \varphi \le 90°$, the surface elements are viewed at a steep angle and the determination of φ is limited by the resolution achieved by the observation system.

Once the values of α and φ have been determined experimentally using the relationships (7) and (9) across an examined object, its 3D geometry can be assembled with corresponding surface elements, whose orientations are specified by the unit normal vectors

$$\vec{n} = \begin{pmatrix} n_x \\ n_y \\ n_z \end{pmatrix} = \begin{pmatrix} \sin(\varphi) \cdot \cos(\alpha) \\ \sin(\varphi) \cdot \sin(\alpha) \\ \cos(\varphi) \end{pmatrix}, \tag{10}$$

see Fig. 2. There are many different approaches for this procedure and a detailed description of the applied method is beyond the scope of the present paper.

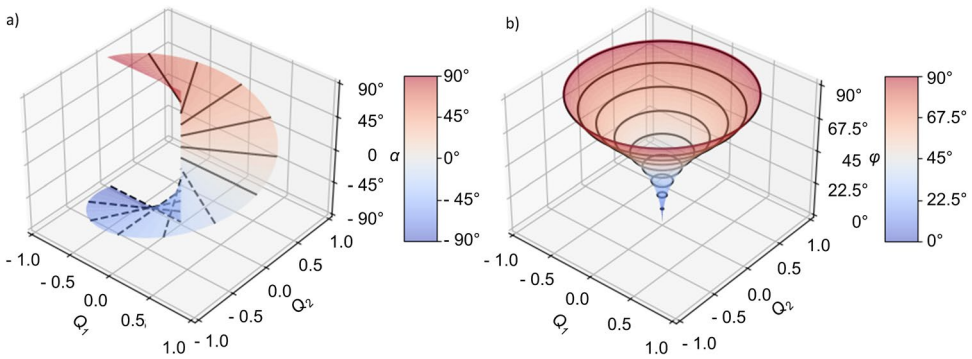

Fig. 4 **a** The azimuthal angle and **b** the polar angle φ as functions of the quotients Q_1 and Q_2, for steel with the refractive index n = 2.95 and extinction coefficient k = 3.48 at the wavelength λ = 857 nm. The black lines are contour lines (dashed for negative values of α)

3 Setup of the 3D polarization goniometer

The patented [22] 3D-Polarization Goniometer consists of a polarizing optics, an imaging system and an evaluation unit. The polarizing optics are integrated into the imaging system. The imaging system creates four images of the process zone, each behind differently oriented linear polarizers. The four images are simultaneously recorded with a high-speed camera. The evaluation unit later calculates the surface angles and the 3D-geometry.

The polarizing optics are shown in Fig. 5. The incident thermal radiation is first split into two paths by a non-polarizing 50% beam splitter cube (dark blue). Adjustable prisms (transparent in Fig. 5) are used to deflect the two beams (red) by total internal reflection. In each of the two paths, the thermal radiation is again separated by polarizing beam splitter cubes (cyan), the orientations of the polarization of the resulting beams with respect to the chosen reference are specified by the labels in the figure. The subsequent mirrors and a second set of polarizing cubes serve to arrange the 4 beams in a square array, before they leave the polarizing optics. In the following, the four generated images will be named according to the corresponding orientation of the polarizers: 0°, 45°, 90° and 135°. The optical path lengths were designed to be the same for all 4 generated beams to facilitate the integration of this polarizing unit into an imaging system, as sketched in Fig. 6.

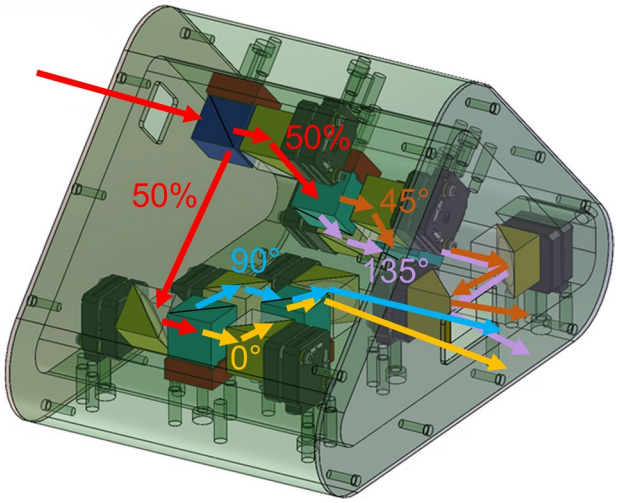

Fig. 5 The polarizing optics split the incoming thermal radiation into four linearly polarized beams with different polarization orientations of 0°, 45°, 90° and 135°

Such a system is used to image the surface of the inspected hot object onto the chip of a high-speed camera for each of the 4 polarized beam paths. Aperture 1 is used to control the exposure (and at the same time the depth of focus), whereas aperture 2 limits the area that is observed on the inspected object to accommodate all 4 images, which need to be separated on the chip of the camera. A band-pass filter centered at a wavelength of $\lambda = 857$ nm with a bandwidth of 30 nm was chosen, because most common metals have no spectral emission lines in this spectral range. The camera used for our experiments was a SA5 from Photron, which allows framerates up to several 100 kHz. The whole setup was encased to avoid disturbances caused by ambient radiation.

When adding optical elements to this setup one needs to take into account the effect that they may have on the polarization of the beams, especially the phase shifts occurring at reflective elements, which can significantly alter the polarization of the interacting beam.

Each image recorded by the high-speed camera is evaluated by an algorithm comprising a local superimposition of the 4 images in each frame, a pixel-wise determination of the angles φ and α, and a reconstruction of the 3D-geometry of the inspected object. These three steps are explained in the following on the basis of the validation experiment.

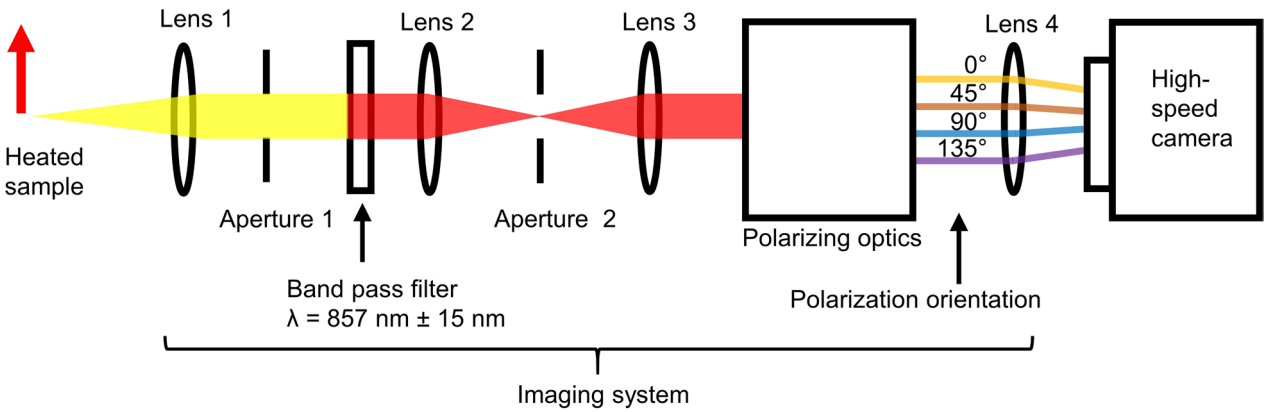

Fig. 6 Imaging system used in connection with the polarizing optics

4 Validation

A steel sphere was heated in a vacuum chamber to validate the optical setup and the determination of the surface angles. The sphere consisted of 1.3505/100Cr6 steel and had a diameter of 1.00 mm. The quality of the sphere was G3 according to DIN 5401/ISO3290, hence the surface roughness Ra was <0.01 µm and the deviation of the diameter was limited to ± 5.32 µm. The sphere was placed on a 1.5 mm thick copper plate with a recess for the sphere. This arrangement was placed in a vacuum chamber with a pressure of $p<3$ mbar to protect the sphere against immediate oxidation by the ambient air, which would alter the emissivity. The sphere was heated by a laser beam, through a top window of the chamber. The laser used for heating the sphere was a TRUDISK 16002 with a wavelength of 1030 nm. The laser was operated at a moderate average power of 330 W. The beam was delivered through a fiber with a core diameter of 200 µm. After leaving the fiber, the beam was first collimated and then focused by means of two lenses, each with a focal length of 200 mm. The beam waist was placed 36 mm above the heated surface of the sphere. The beam's angle of incidence was 3° with respect to the copper plate and the center of the beam was placed at a lateral distance of approximately 2 mm from the sphere. This procedure was chosen to obtain homogeneous heating of the sphere and to avoid melting. The heating time was 6 s.

A side window of the chamber allowed the observation of the heated sphere by means of the 3D-Polarization-Goniometer. The diameter of the three lenses 1, 2, and 3, in Fig. 6, was 1 inch. Lens 4 had a diameter of 2 inches. The focal lengths of the lenses were $f_1=100$ mm, $f_2=100$ mm, $f_3=80$ mm, and $f_4=200$ mm. The complete heating and cooling cycle were recorded with a framerate of 125 fps. An exposure time of 8 ms was used for the camera to obtain a sufficient signal in the single frames. Lower exposure times can be used for objects with higher temperatures and the therefore stronger thermal emission.

Each frame containing the four differently polarized images was saved with a 12-bit grey level. A rigid image registration was performed for the four images. The calculation of the surface angle according to the theory described above assumes that the four beam paths are subject to identical attenuation. As this is usually not the case in practice, the loss factor for each of the four beam paths must be determined first to correct the respective transmitted intensities. The loss factors can be derived by directly comparing the four images of the sphere: Since the polar angle is zero with respect to the observing direction at the center of the sphere, the emissivity/intensity should be the same in all four images.

In order to compensate for the different losses in the 4 beam paths in our setup and to have identical gray values on the center of the sphere in all 4 images, the intensities of the images had to be multiplied by 1.02, 1.33, 1.0 and 1.56 in the images with the polarizer orientations of 0°, 45°, 90° and 135°, respectively. The resulting images, which were recorded immediately after the heating (laser off), are shown in Fig. 7b.

Figure 7 a) shows the theoretically expected intensity distribution behind each of the four polarizers as calculated with Eq. 4 and assuming a refractive index of $n=2.95$ and an extinction coefficient of $k=3.48$ for iron [20]. Comparison of these four intensity distributions with the measured ones shown in Fig. 7b demonstrates a good agreement between theory and experiment.

The polar angle φ and the azimuthal angle α were calculated for each pixel from the experimentally recorded images following the theory with the approximated Fresnel equations presented above, again assuming $n=2.95$ and $k=3.48$. The result is shown in Fig. 8.

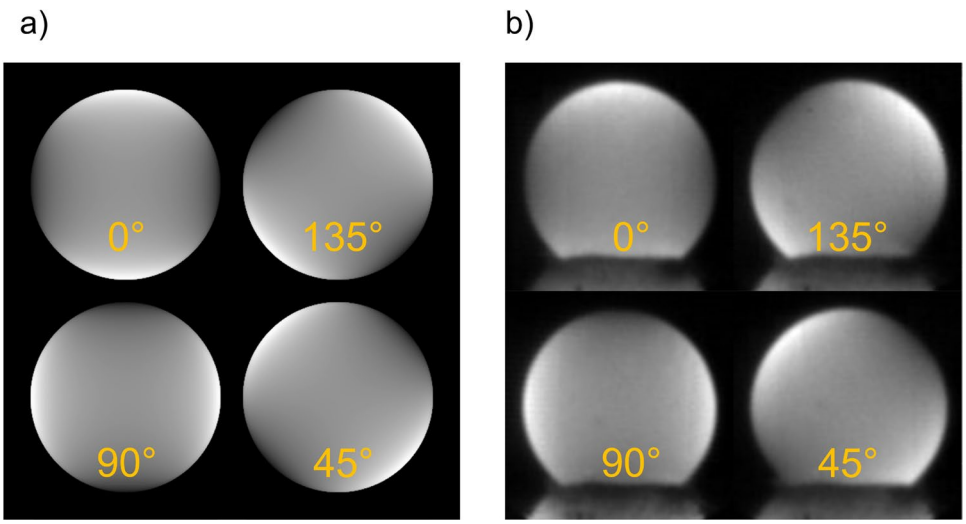

Fig. 7 **a** Calculated intensity distributions of the thermal radiation emitted from a sphere observed through polarizing filters with the marked orientations. **b** Experimentally measured and normalized (loss-corrected) intensity distributions. The bulge at the bottom is the sample holder. The diameter of the sphere was 1.00 mm

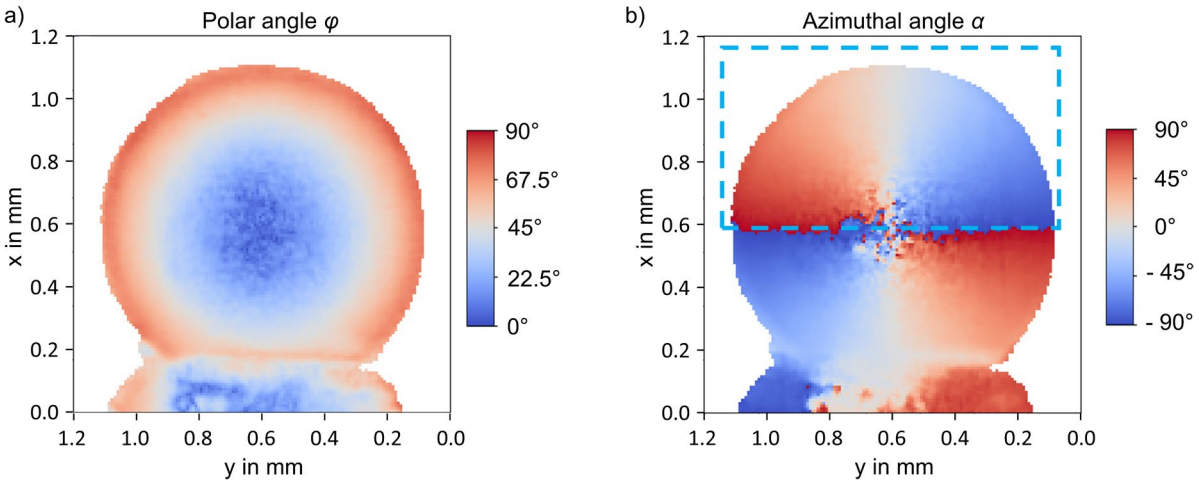

Fig. 8 Polar angle φ (**a**) and azimuthal angle α (**b**) as determined from the measured images in Fig. 7b. The blue dashed rectangle marks the area which was used for the 3D-reconstruction

The polar angle φ increases continuously from the center to the edge of the sphere and is consistent with the expectation for a sphere. Due to the noise in the recorded images and the sensitivity of the reconstruction of the polar angle φ to deviations of the measured intensities explained above, φ was measured to range between 5° to 15° on the center of the sphere instead of the expected 0°. The precision of the measurement is also limited near the edge of the sphere due to the spatial resolution of the camera as differently inclined parts of the surface are imaged onto one single pixel at very steep angles. The highest measurement precision is obtained within the range $15° < \varphi < 70°$ with deviations of typically less than ± 2° from the theoretical value given by the observed spherical surface.

The above-mentioned ambiguity of the determination of the azimuthal angle α is seen in Fig. 8 b) by the fact that the values of α on the lower half of the sphere range between -90° and 90° rather than between ± 90° and ± 180°. The correct reconstruction of the sphere therefore needs additional knowledge about the convexity of the observed surface. This information is typically available in most of real circumstances. Figure 8b furthermore reveals the above-mentioned problem of the abrupt change of the sign of α that occurs for values near ± 90°, see Fig. 4a, as the uncertainty introduced by the noise in the recorded pictures leads to erratic changes of the sign of α near the central horizontal line through the sphere.

The influence that the uncertainty of α has on the reconstruction of the surface's geometry is reduced with decreasing polar angle, since with $\varphi = 0$ the surface is seen at normal incidence no matter which value is chosen for α. However, this advantage is counteracted to some extent by the fact that the polar angle φ can only be determined with reduced precision when it has small values, see above.

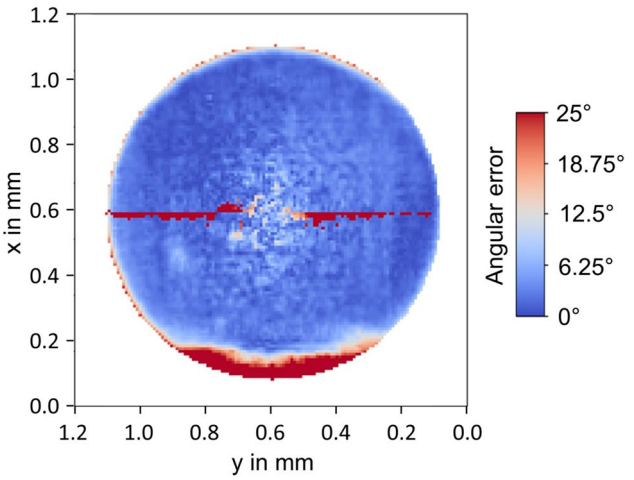

Fig. 9 A map of the angular error between the calculated, and ideal, surface normal angles

The angular error between the calculated surface normal and an ideal surface normal are given in Fig. 9. One can see that the errors are higher directly at the center (see discussion above) and at the outer edge (up to 22°). The large 'errors' towards the bottom of the sphere are due to the inclusion of part of the sample holder in the image (see Fig. 7b). The mean angular error of the upper half of the sphere, which was used for the later reconstruction, is 3.6° with a standard deviation of 2.7°, which is acceptably low.

The 3D shape $z(x, y)$ of the upper half of the sphere, marked by the blue dashed rectangle in Fig. 8 b), was reconstructed using the experimentally determined distributions of the angles φ and α, the result is shown in Fig. 10 a).

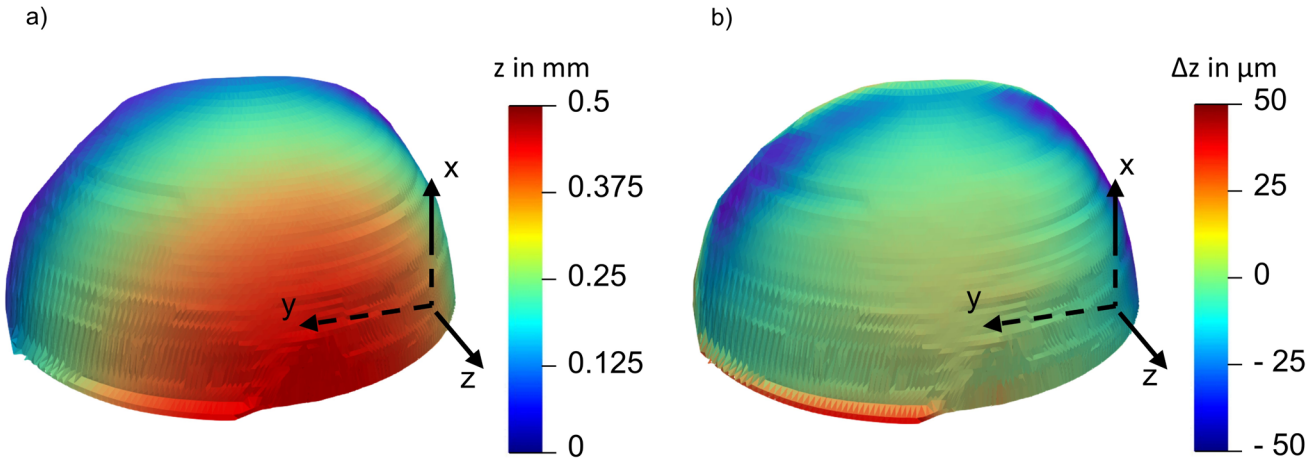

Fig. 10 3D shape of the upper half of the sphere as reconstructed from the 4 polarized images, color-coded with the respective values of z-coordinate of the surface (**a**) and the respective deviation Δz of the reconstructed 3D shape to the ideal sphere (**b**)

The z-coordinate of the center of the sphere at x = 0.6 mm and y = 0.6 mm was arbitrarily set to the value of z = 0.5 mm. As the size and tilt angle of each adjoining pixel is known, the z value of each pixel position can be calculated incrementally from this datum. The impact of the noise in the recorded images on the sign of α for values near ± 90° is clearly seen by the deformation of the reconstructed surface near the lower edge of the depicted upper half of the sphere. Apart from that, the major part of the sphere was reconstructed with good accuracy. Figure 10b shows the color-coded deviation from an ideal sphere as obtained by subtracting the geometry $z_{ideal}(x, y)$ of an ideal sphere from the reconstructed shape. The mean error $\Delta z = z - z_{ideal}$ was found to amount to − 7.3 µm with a standard deviation of 21.5 µm. The results show that the 3D-Polarization Goniometer is well suited for the determination of the 3D shape of a thermally radiating surface as long as they are observed at polar angles between 15° to 75° and azimuthal angles between − 85° and 85°.

With a slightly modified version of the single-frame polarimeter presented here, we were able to perform imaging polarimetry with framerates of up to 75 kHz to investigate the shape of the highly dynamic molten front of the laser cutting process [23]. A sample of the results from this high-speed analysis are presented in Fig. 11. Figure 11a shows the basic experimental set-up with the polarimeter observing the laser cutting front during processing (the right-hand side of the cut material has been removed in this image for clarity). Figure 11b shows the reconstructed morphology of the cutting front at three time intervals, each separated by 13.3

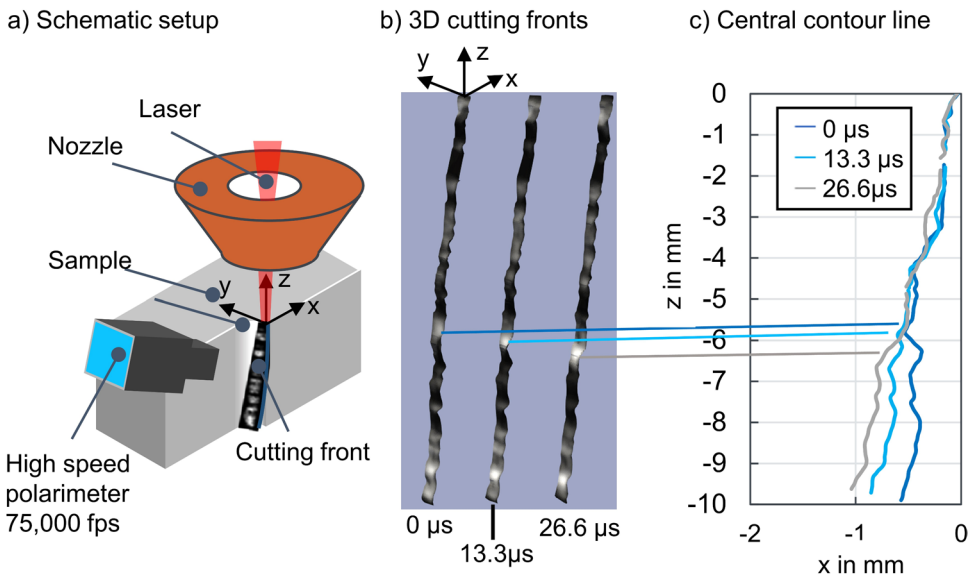

Fig. 11 Results from [23] showing the changes in laser cutting front morphology at a framerate of 75 k Hz. **a** Experimental set-up, **b** cutting front morphology at 13.3 microsecond intervals, **c** center-line profiles of the cutting front (10 mm thick stainless steel cut at 4.5 m/min with a laser power of 8 kW)

microseconds (i.e., framerate was 75 kHz). Figure 11c presents the cutting front as center-line cross section profiles, revealing the dynamic nature of the process. The maximum framerate involved could be increased to several 100 kHz, by using the same equipment with more advanced high-speed cameras with a higher light sensitivity.

5 Conclusion

We have presented the equations that are required to reconstruct the 3D shape of surfaces from 4 images of their thermal emission recorded through linear polarizers with different orientations. The complex refractive index of the observed object must be known for the calculations.

The procedure was validated using an experimental setup with a high-speed camera. The geometric accuracy validation was performed using the example of a heated sphere of steel and it was found that the 3D geometry of the observed surface can be reconstructed with suitable accuracy as long as the surfaces are seen at polar angles between 15° to 75° and azimuthal angles between − 85° and 85°.

The system, which was designed to analyze metal surfaces at or above their melting temperature, has been found to be suitable for monitoring the highly dynamic processing fronts associated with laser material processing (cutting, welding etc.).

Appendix A: Solving Eqs. (5) and (6) for the azimuthal angle $-90° \le \alpha < 90°$

The two Eqs. 5 and 6 can be rearranged to read

$$\frac{\varepsilon_p(\varphi)}{\varepsilon_s(\varphi)} = \frac{\cos(2\alpha) + Q_1(\varphi,\alpha)}{\cos(2\alpha) - Q_1(\varphi,\alpha)} \tag{11}$$

and

$$\frac{\varepsilon_p(\varphi)}{\varepsilon_s(\varphi)} = \frac{\sin(2\alpha) + Q_2(\varphi,\alpha)}{\sin(2\alpha) - Q_2(\varphi,\alpha)}, \tag{12}$$

respectively. The angle φ is eliminated combining the two equations to

$$\frac{\sin(2\alpha) + Q_2(\varphi,\alpha)}{\sin(2\alpha) - Q_2(\varphi,\alpha)} = \frac{\cos(2\alpha) + Q_1(\varphi,\alpha)}{\cos(2\alpha) - Q_1(\varphi,\alpha)}, \tag{13}$$

which can be simplified to

$$tan(2\alpha) = \frac{Q_2(\varphi,\alpha)}{Q_1(\varphi,\alpha)}, \tag{14}$$

which can be used to experimentally determine the azimuthal angle α by replacing $Q_1(\varphi,\alpha)$ and $Q_2(\varphi,\alpha)$ by their measured values $\widehat{Q}_1$ and $\widehat{Q}_2$.

Within the considered range $-90° \le \alpha < 90°$ the ambiguity caused by the periodicity of the trigonometric functions can be solved by considering the signs of the quotients $\widehat{Q}_1$ and $\widehat{Q}_2$. It can be seen from Fig. 3 that for $\widehat{Q}_1 > 0$, α ranges between $-45°$ and $45°$ and hence can be calculated with $arctan\left(\frac{\widehat{Q}_2}{\widehat{Q}_1}\right)/2$. When $\widehat{Q}_2 < 0$ and $\widehat{Q}_1 < 0$, α ranges between $-45°$ and $-90°$. This can be accounted for by adding $-\pi$ to the term $arctan\left(\frac{\widehat{Q}_2}{\widehat{Q}_1}\right)/2$. When $\widehat{Q}_2 > 0$ and $\widehat{Q}_1 < 0$, α ranges between 45° and 90°, which can be accounted for by adding π to the term $arctan\left(\frac{\widehat{Q}_2}{\widehat{Q}_1}\right)/2$. Finally, when $\widehat{Q}_1 = 0\, and\, \widehat{Q}_2 < 0$, $\alpha = -45°$ and when $\widehat{Q}_1 = 0\, and\, \widehat{Q}_2 > 0$, $\alpha = 45°$. Note that α is not defined when both $\widehat{Q}_1 = 0$ and $\widehat{Q}_2 = 0$. This is logical, since according to Figs. 2, 3 this only applies to an uninclined surface with $\varphi = 0$, for which α can adopt any arbitrary value without changing the orientation of the surface.

The above can be summarized by

$$\begin{cases} \dfrac{\arctan\left(\frac{\hat{Q}_2}{\hat{Q}_1}\right)+m\cdot\pi}{2} \begin{cases} m = 0 \text{ for } \hat{Q}_1 > 0 \\ m = -1 \text{ for } \hat{Q}_1 < 0 \text{ and } \hat{Q}_2 < 0 \\ m = 1 \text{ for } \hat{Q}_1 < 0 \text{ and } \hat{Q}_2 > 0 \end{cases} \\ -\frac{\pi}{4} \text{ for } \hat{Q}_1 = 0 \text{ and } \hat{Q}_2 < 0 \\ \frac{\pi}{4} \text{ for } \hat{Q}_1 = 0 \text{ and } \hat{Q}_2 > 0 \\ \text{undefined for } \hat{Q}_1 = 0 \text{ and } \hat{Q}_2 = 0 \\ -\frac{\pi}{2} \text{ for } \hat{Q}_1 < 0 \text{ and } \hat{Q}_2 = 0 \end{cases} \tag{15}$$

In computing and mathematics this is commonly expressed by the atan2 function [21]

$$\alpha = \frac{atan2\left(\frac{\widehat{Q}_2}{\widehat{Q}_1}\right)}{2}. \tag{16}$$

Appendix B: Derivation of the equation for the polar angle φ

By inserting $\varepsilon_p(\varphi)$ from Eq. 1 and $\varepsilon_s(\varphi)$ from Eq. (2) into Eq. (11) and using the measured value $\widehat{Q}_1$ for the quotient Q_1 one finds

$$\frac{\varepsilon_p(\varphi)}{\varepsilon_s(\varphi)} = \frac{\left(n^2+k^2\right) + 2\cdot n\cdot cos(\varphi) + cos^2(\varphi)}{\left(n^2+k^2\right)\cdot cos^2(\varphi) + 2\cdot n\cdot cos(\varphi) + 1} = \frac{\cos(2\alpha) + \widehat{Q}_1}{\cos(2\alpha) - \widehat{Q}_1}. \tag{17}$$

Applying the trigonometric relations $\tan(2\alpha) = \sin(2\alpha)/\cos(2\alpha)$ and $sin^2(2\alpha) + cos^2(2\alpha) = 1$ to

Eq. (14) and inserting the measured values of the quotients one finds

$$\cos(2\alpha) = \sqrt{\frac{\hat{Q}_1^2}{\hat{Q}_1^2 + \hat{Q}_2^2}}. \tag{18}$$

Inserting this into Eq. (17) yields

$$\frac{\left(n^2+k^2\right) + 2\cdot n\cdot cos(\varphi) + cos(\varphi)^2}{\left(n^2+k^2\right)\cdot cos(\varphi)^2 + 2\cdot n\cdot cos(\varphi) + 1} = \frac{1+\sqrt{\hat{Q}_1^2+\hat{Q}_2^2}}{1-\sqrt{\hat{Q}_1^2+\hat{Q}_2^2}}, \tag{19}$$

which does not depend on α anymore. By substituting $\sqrt{\hat{Q}_1^2+\hat{Q}_2^2}$ with r and rearranging Eq. (19) one obtains

$$\begin{aligned}&\cos(\varphi)^2\cdot\left(r\cdot\left(1+n^2+k^2\right)-\left(1-n^2-k^2\right)\right)\\&\quad + cos(\varphi)\cdot(4\cdot n\cdot r) + r\cdot\left(1+n^2+k^2\right)+\left(1-n^2-k^2\right) = 0.\end{aligned} \tag{20}$$

which is solved by

$$\cos(\varphi_\pm) = \frac{-b\pm\sqrt{b^2-4ac}}{2a}, \tag{21}$$

where

$$a = r\cdot\left(1+n^2+k^2\right)-\left(1-n^2-k^2\right), \tag{22}$$

$$b = 4\cdot n\cdot r, \tag{23}$$

$$c = r\cdot\left(1+n^2+k^2\right)+\left(1-n^2-k^2\right), \tag{24}$$

hence

$$cos(\varphi_\pm) = \frac{-2\cdot n\cdot r\pm\sqrt{4\cdot n^2\cdot r^2-\left(r\cdot\left(1+n^2+k^2\right)-\left(1-n^2-k^2\right)\right)\cdot\left(r\cdot\left(1+n^2+k^2\right)+\left(1-n^2-k^2\right)\right)}}{r\cdot\left(1+n^2+k^2\right)-\left(1-n^2-k^2\right)}. \tag{25}$$

Note that within the considered range $0°\le\varphi\le 90°$ the value of $\cos(\varphi)$ is positive, which is obtained by using the solution with the + sign in Eq. (21) and Eq. (25).

Acknowledgements The presented work was funded by the Deutsche Forschungsgemeinschaft (DFG, German Research Foundation) – 431336540 and the DFG project "ELS PoGo" (GR 3172/20-1). The responsibility for this paper is taken by the authors.

Author contributions MS wrote the original draft, performed the experiment, analyzed and visualized the data. MS derived the formulas, supported by PB and refined by TG. The measurement setup was designed by MS and PB. The work was reviewed, edited and supervised by PB, RW, CH and TG.

Funding Open Access funding enabled and organized by Projekt DEAL.

Data availability Data is provided within the manuscript or supplementary information files.

Declarations

Conflict of interest The authors declare no conflicts of interest.

References

1. O. Bocksrocker, P. Berger, F. Fetzer, V. Rominger, T. Graf, Lasers Manuf. Mater. Process. **24**, 52006 (2018)
2. I. Eriksson, J. Powell, A.F.H. Kaplan, Proceeding of ICALEO (2010)
3. K. Hirano, R. Fabbro, J. Laser Appl. **24**, 12006 (2012)
4. Virtual laser cutting simulation for real parameter optimization (JLPS 2016)
5. J. Lind, C. Hagenlocher, D. Blazquez-Sanchez, R. Weber, T. Graf, High-speed X-ray imaging of the melt flow during laser beam cutting, in: S. Kaierle, S.W. Heinemann (eds), High-Power Laser Materials Processing: Applications, Diagnostics, and Systems XI (SPIE 2022–2022)
6. H. Ozaki, M.Q. Le, H. Kawakami, J. Suzuki, Y. Uemura, Y. Doi, M. Mizutani, Y. Kawahito, J. Mater. Process. Technol. **237**, 181 (2016)
7. F. Bernhard (ed), Technische Temperaturmessung. Physikalische und meßtechnische Grundlagen, Sensoren und Meßverfahren, Meßfehler und Kalibrierung ; Handbuch für Forschung und Entwicklung, Anwendungenspraxis und Studium ; mit 297 Tabellen und 202 Berechnungsbeispielen (Springer, Berlin 2004)
8. J.S. Tyo, D.L. Goldstein, D.B. Chenault, J.A. Shaw, Appl. Opt. **45**, 5453 (2006)
9. N. Coniglio, A. Mathieu, O. Aubreton, C. Stolz, Opt. Lett. **38**, 2086 (2013)
10. M. Sawannia, P. Berger, R. Weber, T. Graf, I.O.P. Conf, Ser. Mater. Sci. Eng. **1135**, 12013 (2021)
11. M. Sawannia, P. Berger, M. Jarwitz, R. Weber, T. Graf, Proceeding of ICALEO (2018)

12. M. Sawannia, P. Berger, M. Jarwitz, R. Weber, T. Graf, Lasers in manufacturing conference (2019)
13. M. Sawannia, S. Jakobs, S. Gach, S. Olschok, R. Weber, T. Graf, Proceeding of ICALEO (2022)
14. A.M. Prohorov, V.I. Konov, Laser heating of metals. [By] A. M. Prokhorov, V. I. Konov etc (XIX, Bristol—Philadelphia—New York 1990)
15. A. Michalowski, Untersuchungen zur Mikrobearbeitung von Stahl mit ultrakurzen Laserpulsen. Zugl.: Stuttgart, Univ., Diss., 2014 (Utz, München 2014)
16. F. Dausinger, Strahlwerkzeug Laser: Energiekopplung und Prozesseffektivität. Zugl.: Stuttgart, Univ., Habil.-Schr (Teubner, Stuttgart 1995)
17. O. Bocksrocker, Berger Peter, T. Hesse, Boley Meiko, Graf Thomas, Proceedings of the 8th International WLT Conference on Lasers in Manufacturing LiM (2015)
18. J. Weberpals, T. Hermann, P. Berger, H. Singpiel, Phys. Procedia **12**, 704 (2011)
19. F.A. Jenkins, H.E. White, *Fundamentals of optics* (McGraw-Hill, Chennai, 1976)
20. P. Johnson, R. Christy, Phys. Rev. B **9**, 5056 (1974)
21. Weitz, Konkrete Mathematik (nicht nur) für Informatiker (Springer Fachmedien Wiesbaden 2018)
22. P. Berger, J.-P. Weberpals, F. Abt, T. Graf, Use of the polarization of thermal radiation for the detection of 3D structures. B23K 26/03 (2006.01) (2010)
23. M. Sawannia, M. Borkmann, P. Herwig, A. Wetzig, R. Weber, T. Graf, Procedia CIRP **111**, 736 (2022)